

Highly efficient quantum Stirling engine using multilayer Graphene

Bastian Castorene,^{1,2,*} Francisco J. Peña,² Eric Suárez Morell,²
Caio Lewenkopf,³ Martin HvE Groves,^{1,2} Natalia Cortés,² and Patricio Vargas²

¹*Instituto de Física, Pontificia Universidad Católica de Valparaíso, Casilla 4950, 2373223 Valparaíso, Chile*

²*Departamento de Física, Universidad Técnica Federico Santa María, 2390123 Valparaíso, Chile*

³*Instituto de Física, Universidade Federal do Rio de Janeiro, Rio de Janeiro, RJ 21941-972, Brazil*

(Dated: March 13, 2026)

In this work, quantum Stirling engines based on monolayer, AB-stacked bilayer, and ABC-stacked trilayer graphene under perpendicular magnetic fields are analyzed. Performance maps of the useful work (ηW) reveal a robust optimum at low magnetic fields and moderately low temperatures, with all stackings capable of reaching Carnot efficiency under suitable configurations. The AB bilayer achieves this across the broadest parameter window while sustaining finite work, the monolayer exhibits highly constrained regimes, and the trilayer shows smoother trends with sizable ηW . These results identify multilayer graphene, particularly the AB bilayer, as a promising platform for efficient Stirling engines, while also highlighting the versatility of the monolayer in realizing all four operational regimes of the Stirling cycle.

I. INTRODUCTION

Quantum thermodynamics examines how the fundamental principles of energy transfer, heat exchange, and entropy apply to small systems where quantum effects such as coherence, entanglement, spin correlations, and discrete energy levels give rise to thermodynamical properties with no classical counterpart, and where quantum statistics provides a natural framework to describe these phenomena [1–13].

In this context, considerable attention has been devoted to understanding how quantum systems, such as trapped ions, superconducting qubits, quantum dots [14–19], and low-dimensional electronic materials and their diverse behaviors can be harnessed to implement heat engines capable of producing useful work. Among quantum thermal machines, the Stirling cycle has attracted particular interest due to its potential to achieve high efficiency in regimes where thermalization and isochoric processes can be controlled with precision [20–32]. In light of these considerations, theoretical and experimental investigations have shown that quantum heat engines based on discrete energy spectra may surpass their classical counterparts in specific regimes, particularly when the working substance exhibits a tunable energy level structure and distinctive statistical properties [33, 34].

Graphene and its multilayer stacks, when subjected to perpendicular magnetic fields [35–39] stand out as promising platforms for quantum heat engines. Beyond their ease of fabrication and high degree of experimental control [40–45], manifestations of their quantized spectrum are robust against temperature, since these systems exhibit quantum Hall plateaus even at room temperatures under sufficiently high magnetic fields [46] – a critical feature for practical applications. Furthermore, the large degeneracy of the Landau levels (LL) involves a

macroscopic number of participating electrons, N , even in micron-size flakes [39]. This provides a unique framework to explore quantum corrections to thermodynamic quantities stemming from the discrete Landau-level spectrum, while remaining within the thermodynamic limit. Consequently, the small- N thermal fluctuations typically found in few-body systems (both classical and quantum) are suppressed, making it possible to isolate genuine quantum effects. Very importantly, when driven by a varying magnetic field B , these quantum systems – unlike most others – avoid the dissipation associated to Landau-Zener transitions [47, 48], as Landau levels do not cross with changes in B . Finally, like other two-dimensional materials, the chemical potential (or doping) can be precisely tuned via electrostatic gating, offering a robust mechanism for controlling the engine’s working fluid.

Several studies have proposed graphene-based systems, including quantum dots and multilayer structures, as promising candidates for quantum engines [49–56]. While these pioneering works offer valuable insights, they predominantly rely on Boltzmann statistics [7, 50, 51, 57]. By neglecting the fermionic nature of the electronic working fluid and assuming charge neutrality, the lack of quantitative accuracy of their results and the narrow focus of their setting call for a reexamination.

This study examines a quantum Stirling cycle implemented in monolayer, AB-stacked bilayer, and ABC-stacked trilayer graphene under perpendicular magnetic fields as the working medium. Employing a low-energy Landau-level description and Fermi–Dirac statistics at finite doping, we correct the previous studies, expand their scope beyond the charge-neutrality point, and provide a thermodynamic analysis more closely aligned with experimentally accessible conditions [58, 59]. Within a grand-canonical framework, we evaluate key observables such as internal energy and entropy while explicitly accounting for the degeneracies specific to each multilayer configuration.

A central motivation of this work is to clarify how

* bastian.castorene.c@mail.pucv.cl

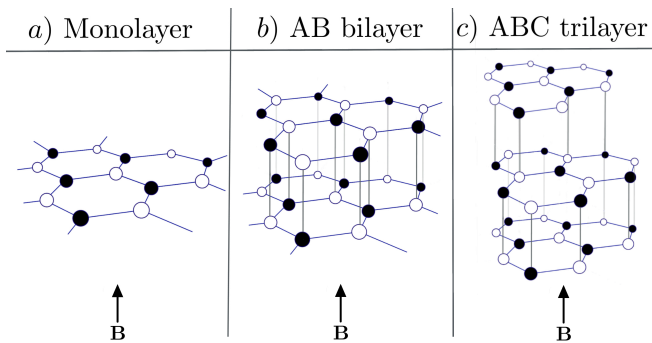


FIG. 1: Schematic representation of the lattice structure of graphene multilayer systems (under a perpendicular homogeneous magnetic field B). Panel (a) shows the monolayer, panel (b) the AB-stacked bilayer, and panel (c) the ABC-stacked trilayer.

the microscopic Landau-level structure of mono-, bi-, and trilayer graphene shapes the performance of a quantum Stirling cycle. We show that the stacking-dependent spectra of these multilayers can naturally produce parameter regimes in which the Stirling efficiency approaches the Carnot bound while still delivering a finite amount of energy per cycle in the reversible, quasistatic limit (and thus zero power), without relying on quantum criticality or ideal regenerative mechanisms. This highlights the role of stacking order as a physically meaningful variable for controlling the thermodynamic response of quantum heat engines.

The structure of the paper is as follows. Section II introduces the theoretical framework and the Landau level spectra for graphene with different multilayer stackings. Section III derives the thermodynamic functions required to implement the Stirling cycle. Section IV presents the analysis of efficiency and work output across different regimes. Finally, Sec. V presents the conclusions with a summary and possible extensions.

II. THEORY AND METHODS

A. Landau Level Spectrum in Multilayer Graphene

At low electronic doping, the low-energy LL spectra of mono-, AB-bilayer, and ABC-trilayer graphene in a perpendicular magnetic field (as shown in Fig. 1) can be cast into a single compact form that highlights the multilayer scalings [35–38, 45].

Introducing a stacking index J ($J = 1$ monolayer, $J = 2$ AB bilayer, $J = 3$ ABC trilayer), we write

$$\varepsilon_{n,\pm}^{(J)} = \pm \hbar \omega_c^{(J)} \sqrt{\prod_{j=0}^{J-1} (n-j)}, \quad n = 0, 1, 2, \dots, \quad (1)$$

where n is the LL index and \pm indicate conduction and valence band LLs. The J -dependent cyclotron frequency

$\omega_c^{(J)}$ encodes the microscopic parameters of each system. As we show below, Eq. (1) yields the characteristic magnetic-field scaling

$$\varepsilon_n^{(J)} \propto B^{J/2}, \quad (2)$$

and predicts J zero-energy modes ($n = 0, 1, \dots, J-1$). Consequently, the effect spin, valley and zero-energy level degeneracies results in a combined degeneracy $g_n^{(J)} = 4$ for all levels with $n \geq 1$ and

$$g_0^{(1)} = 4, \quad g_0^{(2)} = 8, \quad g_0^{(3)} = 12. \quad (3)$$

for $n = 0$.

For the three cases addressed here, the corresponding LL energies are given by

$$J = 1: \quad \varepsilon_{n,\pm}^{(1)} = \pm \hbar \omega_c^{(1)} \sqrt{n}, \quad (4)$$

$$\hbar \omega_c^{(1)} = \sqrt{2e\hbar v_F^2 B} \approx 36.3 \sqrt{B} \text{ meV},$$

$$J = 2: \quad \varepsilon_{n,\pm}^{(2)} = \pm \hbar \omega_c^{(2)} \sqrt{n(n-1)}, \quad (5)$$

$$\hbar \omega_c^{(2)} = \frac{2e\hbar v_F^2 B}{t_\perp} \approx 4.77 B \text{ meV},$$

$$J = 3: \quad \varepsilon_{n,\pm}^{(3)} = \pm \hbar \omega_c^{(3)} \sqrt{n(n-1)(n-2)}, \quad (6)$$

$$\hbar \omega_c^{(3)} = \frac{(2eB\hbar v_F^2)^{3/2} \sqrt{\hbar}}{t_\perp^2} \approx 0.771 B^{3/2} \text{ meV},$$

where the magnetic field B is measured in tesla. Here, v_F denotes the Fermi velocity of graphene and t_\perp represents the interlayer hopping amplitude for each system, which characterizes the electronic coupling between adjacent graphene layers. Equations (4) to (6) establish distinct characteristic scales of the Landau-level spectra in multilayer graphene systems. These differences are ultimately manifest in the thermodynamic properties discussed next.

III. THERMODYNAMIC DESCRIPTION OF MULTILAYER GRAPHENE SYSTEMS UNDER MAGNETIC FIELD

A. Grand canonical formalism

In recent studies using graphene as a thermal machine, the thermodynamic behavior of graphene multilayers has been investigated through thermal states based on the canonical ensemble and Landau-level spectra [51, 56], neglecting the fermionic nature of the working fluid. In contrast, in this manuscript the thermodynamic properties of electrons in graphene multilayer systems under perpendicular magnetic fields are naturally described within the grand-canonical ensemble using Fermi–Dirac statistics, where both the temperature T and the chemical potential μ serve as control parameters.

In this framework, the central quantities of interest are the internal energy U , the entropy S , and the particle number $\langle N \rangle$, which together determine the efficiency and work output of thermal cycles.

For multilayer graphene with quantized Landau levels $\varepsilon_{n,\pm}^{(J)}$, the grand-canonical partition function can be written explicitly as

$$\mathcal{Z}^{(J)} = \prod_{n,\pm} \left[1 + e^{-\beta(\varepsilon_{n,\pm}^{(J)} - \mu)} \right]^{g_n^{(J)}}, \quad (7)$$

Taking the degeneracies into account, the grand potential can be expressed as

$$\Omega^{(J)} = -k_B T \sum_{n,\pm} g_n^{(J)} \ln \left[1 + e^{-\beta(\varepsilon_{n,\pm}^{(J)} - \mu)} \right], \quad (8)$$

where $\beta = \frac{1}{k_B T}$. The grand potential gives

$$\begin{aligned} \langle N \rangle &= - \left. \frac{\partial \Omega^{(J)}}{\partial \mu} \right|_T, \quad S = - \left. \frac{\partial \Omega^{(J)}}{\partial T} \right|_\mu, \\ U &= \Omega^{(J)} + TS + \mu \langle N \rangle. \end{aligned} \quad (9)$$

Equivalently, one may start from the Fermi–Dirac distribution, which gives the occupation of each single-particle state $f(\varepsilon, \mu, T) = [e^{\beta(\varepsilon - \mu)} + 1]^{-1}$ together with the density of states (DOS),

$$\nu^{(J)}(\varepsilon) = \sum_{n,\pm} g_n^{(J)} \delta(\varepsilon - \varepsilon_{n,\pm}^{(J)}), \quad (10)$$

which does not yet include the LL orbital degeneracy, that is to be discussed in the next section. These allow the same observables to be written as

$$\langle N(T, B, \mu) \rangle = \int_{-\infty}^{\infty} d\varepsilon \nu^{(J)}(\varepsilon) f(\varepsilon, \mu, T), \quad (11)$$

$$U(T, B, \mu) = \int_{-\infty}^{\infty} d\varepsilon \nu^{(J)}(\varepsilon) \varepsilon f(\varepsilon, \mu, T), \quad (12)$$

$$S(T, B, \mu) = -k_B \int_{-\infty}^{\infty} d\varepsilon \nu^{(J)}(\varepsilon) [f \ln f + (1-f) \ln(1-f)]. \quad (13)$$

Both approaches are formally equivalent: the discrete-level formulation based on the grand potential and the continuum representation using the DOS combined with the Fermi–Dirac distribution, both yielding to identical thermodynamic quantities. It is worth emphasizing that the DOS representation makes explicit the role of Landau-level degeneracies, particularly the zero-energy states in all systems. We adopt the latter approach for our calculations. To guarantee numerical stability across the entire parameter space, the sums over Landau levels

are truncated at a cutoff index of $n = 2000$, or when the relative difference between consecutive evaluations falls below 10^{-6} . Crucially, for the specific temperature and magnetic field regimes considered, thermal population is confined to the lowest levels, with contributions from $n > 20$ being exponentially suppressed. Consequently, the effective number of participating states is limited to $n \lesssim 20$, which is fully consistent with the δ -function DOS representation employed in this work [60].

B. Energy Scales and Parametrization of the Chemical Potential

Having established the theoretical framework, we now estimate the order of magnitude of the energy separation between the ground state and the first accessible Landau excitation as the magnetic field B is varied. This quantity $\hbar \omega_c^{(J)}$ sets the relevant energy scale for the thermodynamic analysis, since it determines the temperatures required to thermally populate excited states as the field is varied [35–37, 45].

For reference to experimental scales, we provide an estimate obtained from the magnetic length, $\ell_B = \sqrt{\hbar/(eB)}$ [35, 39]. By defining N_e as the number of electrons within the magnetic length area $\pi \ell_B^2$, the sheet density can be written as

$$n_{2D} \approx \frac{eB}{\pi \hbar} N_e \simeq 4.86 \times 10^{10} N_e B \text{ cm}^{-2}. \quad (14)$$

Typical electron concentrations in graphene vary according to the substrate and doping, with values ranging from near-neutral (around 10^{12} cm^{-2}) up to $10^{13} - 10^{14} \text{ cm}^{-2}$ for doped samples [61, 62]. Consequently, a standard $1 \mu\text{m}^2$ sample with $n_{2D} \approx 10^{13} \text{ cm}^{-2}$ contains $\simeq 10^5$ electrons in the conduction band. For the purpose of our numerical analysis under modest magnetic fields ($B \approx 1$ T), these experimental scales constrain the modeled particle count to $N_e \lesssim 25$.

Fig. 2 provides an overview of the relation between the magnetic field B , the chemical potential μ , and the resulting particle number N_e for mono-, bi-, and trilayer graphene at fixed temperature of $T = 50$ K. In this figure, N_e is not fixed; instead, we map the full surface $N_e(50, B, \mu)$ in order to illustrate how the distinct Landau-level structures of each multilayer system shape the dependence of the particle number on μ and B . This exploration helps visualize the scaling behaviors originating from the linear, quadratic, and cubic dispersions of the three stackings.

To make a consistent comparison across all layers, the chemical potential is determined self-consistently from the particle-number constraint

$$N_e = \frac{\langle N(T, B, \mu(T, B)) \rangle}{\pi \ell_B^2} = \text{constant}, \quad (15)$$

so that $\mu(T, B)$ is obtained at every point of the thermodynamic cycle. Within this framework, the fixed

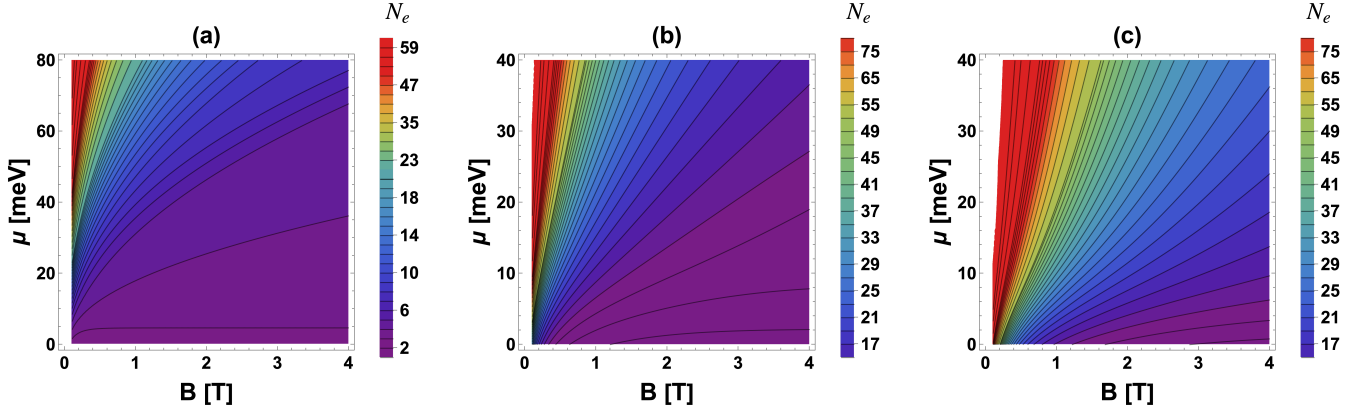


FIG. 2: Color map of N_e as a function of magnetic field B [T] and chemical potential μ [meV] for (a) monolayer, (b) bilayer and (c) trilayered graphene system under a fixed temperature $T = 50$ K.

particle number N_e fully determines the temperature and magnetic-field dependence of the chemical potential, and no additional analytical assumption regarding its T -dependence is imposed.

We emphasize that, for fixed B , the chemical potential also acquires a (comparatively weaker) dependence on temperature, i.e., $\mu = \mu(T, B)$ is determined self-consistently throughout the cycle. This temperature dependence is fully included in our numerical evaluation of the thermodynamic quantities.

C. Thermodynamic Properties: Internal Energy and Entropy of Multilayer Graphene

Having established the Landau-level spectra in Eqs. 4, 5, and 6, together with the parametrized chemical potential of Eq. 15 that ensures a fixed particle number across all three systems. We now turn to the analysis of thermodynamic quantities directly relevant for the operation of quantum heat engines. In particular, we investigate how each multilayer configuration responds under thermal cycling, an aspect of central importance for the implementation of the Stirling cycle.

The internal energy $U(T, B, \mu(T, B))$ of monolayer, bilayer, and trilayer graphene is presented in Fig. 3 as a function of temperature for several fixed magnetic-field values, at constant particle number $N_e = 15$.

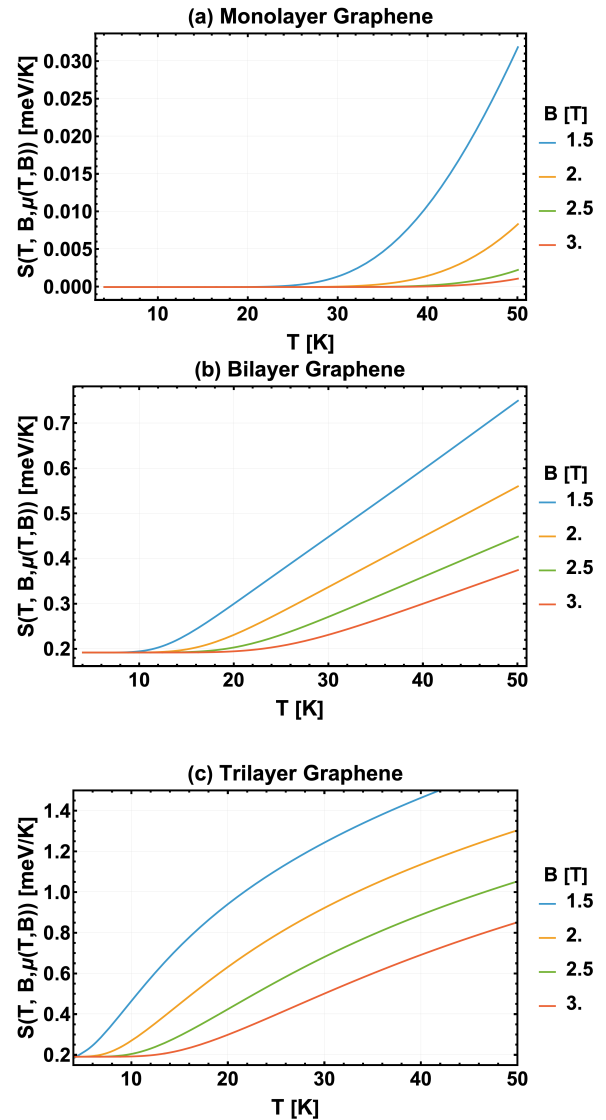


FIG. 4: Entropy $S(T, B, \mu(T, B))$ as a function of temperature for (a) monolayer, (b) bilayer, and (c) trilayer graphene at different magnetic fields, with the particle number fixed at $N_e = 15$.

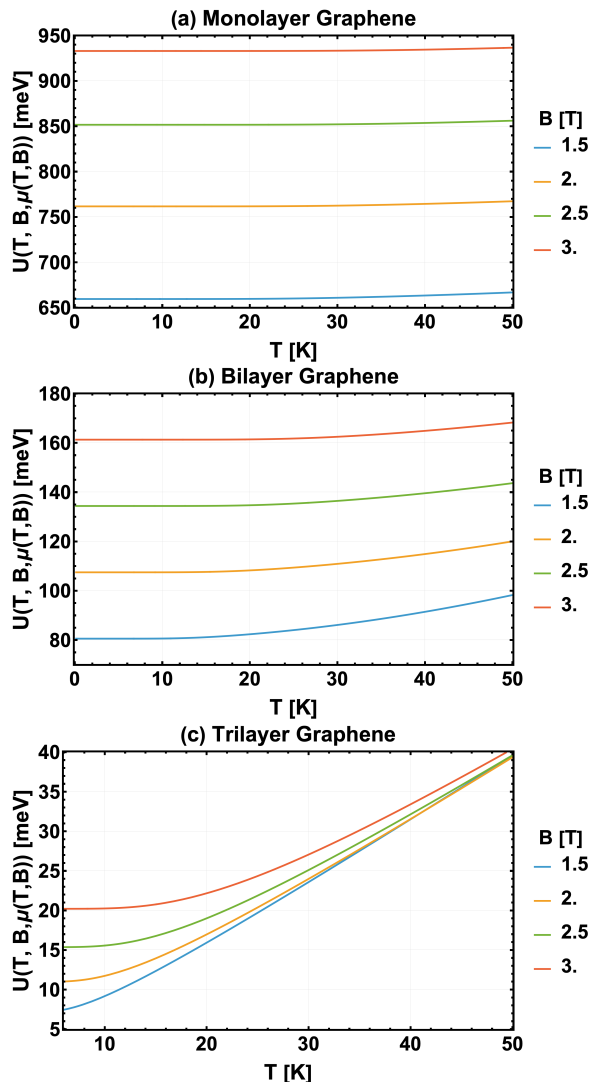


FIG. 3: Internal energy $U(T, B, \mu(T, B))$ as a function of temperature for (a) monolayer, (b) bilayer, and (c) trilayer graphene at different magnetic fields, with the particle number fixed at $N_e = 15$.

In the monolayer case, shown in Fig. 3(a), the internal energy increases moderately with temperature, following a smooth and weakly nonlinear trend. This behavior reflects the relativistic nature of Dirac fermions and the square-root spacing of the Landau levels. Increasing the magnetic field enhances the Landau-level separation, which produces an upward shift in the baseline of internal energy, while the overall temperature dependence remains predominantly sublinear. For the range of fields considered, the internal energy varies between approximately 600 and 950 meV. In Fig. 3(b), the bilayer system exhibits a more pronounced curvature compared to the monolayer, particularly at intermediate temperatures. At lower magnetic fields, the internal energy rises more rapidly with temperature, consistent with the parabolic band structure and the enhanced density of

states near charge neutrality. Because of the smaller Landau-level separations, the states are more easily populated than in the monolayer, which increases the sensitivity of the internal energy to thermal excitations. The overall magnitude of internal energy varies between approximately 80 and 170 [meV] across the magnetic-field range considered.

In Fig. 3(c), trilayer graphene exhibits a qualitatively distinct behavior. At high temperatures, all curves display an approximately linear increase in internal energy with comparable slopes, largely independent of the magnetic field. Similar to the monolayer and bilayer cases, the separation between different B values persists throughout the entire range, with the distinction being most evident at low temperatures, indicating that magnetic-field effects remain relevant despite thermal excitations. This behavior reflects the denser and more intricate low-energy spectrum of the trilayer, which enhances the internal energy under stronger fields. Overall, the temperature dependence of the internal energy in trilayer graphene arises from a competition between two effects: the magnetic field increases the spacing between Landau levels, thereby reducing the number of thermally accessible states and suppressing the growth of internal energy; in contrast, raising the temperature promotes the occupation of higher-energy states, leading to an overall increase in internal energy. Within the explored temperature window, no crossover or inversion is observed among the curves for different magnetic fields, suggesting that neither mechanism fully dominates.

The next discussion focuses on the entropy to further characterize the thermodynamic response. Fig. 4 presents the temperature dependence of the entropy $S(T, B, \mu(T, B))$ for monolayer, bilayer, and trilayer graphene at different magnetic fields, with the particle number fixed at $N_e = 15$. While all three systems exhibit a monotonic increase of entropy with temperature, notable differences arise in magnitude, curvature, and sensitivity to the magnetic field, underscoring the distinct thermodynamic responses of each multilayer configuration. In Fig. 4(a), the entropy of monolayer graphene remains negligible at low temperatures and begins to rise appreciably only above $T \simeq 25$ K, where thermal excitations populate higher Landau levels. The increase is markedly nonlinear, particularly at lower magnetic fields. This behavior reflects the relativistic Landau-level structure where stronger magnetic fields enlarge the spacing between energy levels and thereby suppress thermal activation. Consequently, higher fields substantially reduce the entropy and produce a clear separation among the curves.

In Fig. 4(b), the bilayer case exhibits a more regular and approximately linear increase of entropy with temperature throughout the explored range. The entropy rises from about 0.2 meV/K to nearly 0.75 meV/K at the lowest field $B = 1.5$ T. The larger values compared to the monolayer reflect the denser Landau-level structure associated with the parabolic dispersion. Sensitivity to

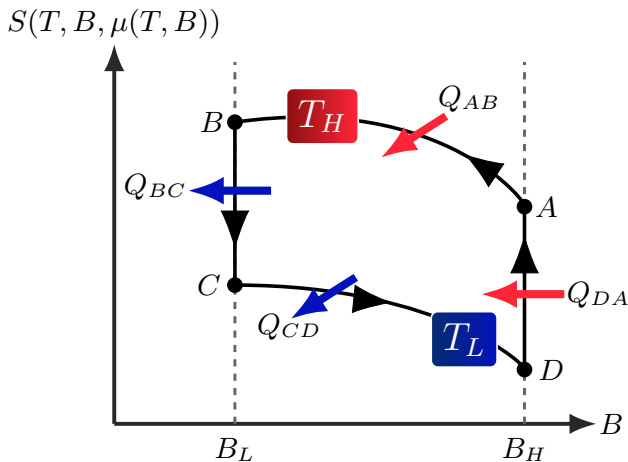


FIG. 5: Diagram of the quantum Stirling cycle in terms of entropy $S(T, B, \mu(T, B))$ for fixed particle-number N_e and the perpendicular magnetic field B . Curves AB and CD correspond to the isotherms at $T = T_H$ and $T = T_L$, respectively. As the magnetic field increases at fixed temperature, the entropy decreases, and vice versa.

the magnetic field is also more pronounced, as stronger fields systematically shift the curves downward.

For the trilayer configuration shown in Fig. 4(c), the entropy starts near 0.2 meV/K and grows beyond 1.3 meV/K for $B = 1.5$ T, displaying a rapid and non-linear increase with temperature. The entropy curves exhibit a strong dependence on the magnetic field. This behavior originates from the cubic low-energy dispersion, which generates a high density of states and reduces the spacing between adjacent energy levels, effectively producing a quasi-continuous spectrum that remains thermally active even under stronger magnetic fields.

1. Quantum Stirling Cycle

The quantum Stirling cycle, illustrated in Fig. 5, consists of four strokes: two isothermal and two isomagnetic processes. In this framework, the perpendicular magnetic field B acts as the external control parameter, while the working substance remains in thermal equilibrium with the reservoirs throughout the entire cycle. For each pair of values (T, B) , the chemical potential $\mu(T, B)$ is determined self-consistently to keep the particle number N_e fixed, and the resulting value is then used in all thermodynamic quantities. The sequence of strokes is as follows:

- **(A \rightarrow B)** Isothermal expansion at temperature T_H , with the magnetic field decreasing from B_H to B_L ,
- **(B \rightarrow C)** Isomagnetic cooling at fixed $B = B_L$, with the temperature lowered from T_H to T_L ,
- **(C \rightarrow D)** Isothermal compression at temperature T_L , with the magnetic field increasing from B_L to B_H ,

TABLE I: Sign convention for heat and work: $W > 0$ for work output, $W < 0$ for input; $Q > 0$ for heat absorbed, $Q < 0$ for heat released by the system.

Operational regime	W	Q_{out}	Q_{in}
Engine	> 0	< 0	> 0
Refrigerator	< 0	> 0	< 0
Accelerator	< 0	< 0	> 0
Heater	< 0	< 0	< 0

- **(D \rightarrow A)** Isomagnetic heating at fixed $B = B_H$, with the temperature raised from T_L back to T_H .

The heat exchanged during each stage is expressed as

$$Q_{AB} = T_H [S(T_H, B_L, \mu(T_H, B_L)) - S(T_H, B_H, \mu(T_H, B_H))], \quad (16)$$

$$Q_{CD} = T_L [S(T_L, B_H, \mu(T_L, B_H)) - S(T_L, B_L, \mu(T_L, B_L))], \quad (17)$$

$$Q_{BC} = U(T_L, B_L, \mu(T_L, B_L)) - U(T_H, B_L, \mu(T_H, B_L)), \quad (18)$$

$$Q_{DA} = U(T_H, B_H, \mu(T_H, B_H)) - U(T_L, B_H, \mu(T_L, B_H)), \quad (19)$$

where the labels L and H are used to distinguish the low and high values of B and T . Invoking the first law of thermodynamics, the total heat absorbed Q_{in} , the heat released Q_{out} , and the net work W per cycle can be expressed as

$$Q_{\text{in}} = Q_{AB} + Q_{DA}, \quad (20)$$

$$Q_{\text{out}} = Q_{BC} + Q_{CD}, \quad (21)$$

$$W = Q_{\text{in}} + Q_{\text{out}}. \quad (22)$$

The convention adopted here is that $Q > 0$ corresponds to heat absorbed by the system, while $W > 0$ indicates net work performed by the system. Within this framework, the efficiency of the cycle is given by

$$\eta = \frac{W}{Q_{\text{in}}} = 1 - \left| \frac{Q_{BC} + Q_{CD}}{Q_{AB} + Q_{DA}} \right|. \quad (23)$$

The physical significance of these expressions is clarified when related to the entropy behavior discussed in Sec. III C, which shows that entropy increases as the external magnetic field decreases at fixed temperature. This guarantees that the isothermal expansion stroke (A \rightarrow B), performed from B_H to B_L , corresponds to a positive entropy change $\Delta S > 0$, and thus a positive heat input $Q_{AB} > 0$. In contrast, the isothermal compression stroke (C \rightarrow D), carried out at lower temperature and in the reverse direction $B_L \rightarrow B_H$, yields a negative entropy change and therefore a negative heat exchange $Q_{CD} < 0$. Consequently, the different operational regimes of the engine are governed entirely by the heat contributions during the isomagnetic strokes (B \rightarrow C and D \rightarrow A).

Table I summarizes the adopted sign convention for heat and total work across the four operational regimes

considered. In this convention, a positive total work $W > 0$ indicates that the system delivers work to the surroundings, whereas $W < 0$ corresponds to work being supplied to the system. Similarly, a positive heat $Q > 0$ denotes energy flowing into the working substance, while $Q < 0$ represents heat released to the external reservoirs. Under these definitions, an engine operates with $W > 0$, absorbing heat from the hot reservoir ($Q_{\text{in}} > 0$) and rejecting heat to the cold one ($Q_{\text{out}} < 0$).

If, under the same parameters, the cycle is run in the reverse (clockwise) direction relative to Fig. 5, the device operates as a refrigerator. In this case, external work input ($W < 0$) is required to extract heat from the cold reservoir ($Q_{\text{out}} > 0$) and release it to the hot reservoir ($Q_{\text{in}} < 0$).

Beyond these two classical regimes, previous studies have shown that the quantum Stirling cycle may also operate in two additional regimes that arise purely from its quantum character [25, 30, 63–65]. In the *accelerator* regime, both the total work and the heat released to the cold reservoir are negative, indicating that external work input is accompanied by simultaneous heating of both reservoirs. In the *heater* regime, all heat flows are negative and $W < 0$, so that the external work is entirely dissipated as heat into both reservoirs. Importantly, these operational regimes are not exclusive to intrinsic properties of stacked graphene systems. It has been shown that twisted bilayer graphene, when employed as a Stirling engine at temperatures within 50 to 150 K, can also exhibit this diversity of thermodynamic behaviors [56].

As will be shown in later sections, the exotic thermodynamic properties of the system, which arise from the constraint of particle number conservation, can induce these additional operational regimes.

IV. RESULTS

A. Stirling Engine Efficiency

In this section, the efficiency of the Stirling engine defined in Eq. (23) and illustrated in Fig. 5 is examined. The working substances correspond to the stacked graphene systems of Fig. 1, with the chemical potential parametrized along all strokes of the cycle to maintain a fixed particle number $N_e \in \{5, 8, 15\}$.

To quantify these effects, Fig. 6 presents the efficiency η as a function of the low magnetic field B_L for monolayer, bilayer, and trilayer graphene. For each configuration, the high magnetic field B_H and the bath temperatures T_L and T_H are kept constant as indicated in the panel captions, while the Carnot efficiency $\eta_C = 1 - T_L/T_H$ is shown as a horizontal red reference line.

In the monolayer case shown in Fig. 6(a), the conditions for the system to operate as an engine are strongly constrained for thermal reservoirs at $T_L = 50.7$ K and $T_H = 53.85$ K, corresponding to a Carnot efficiency

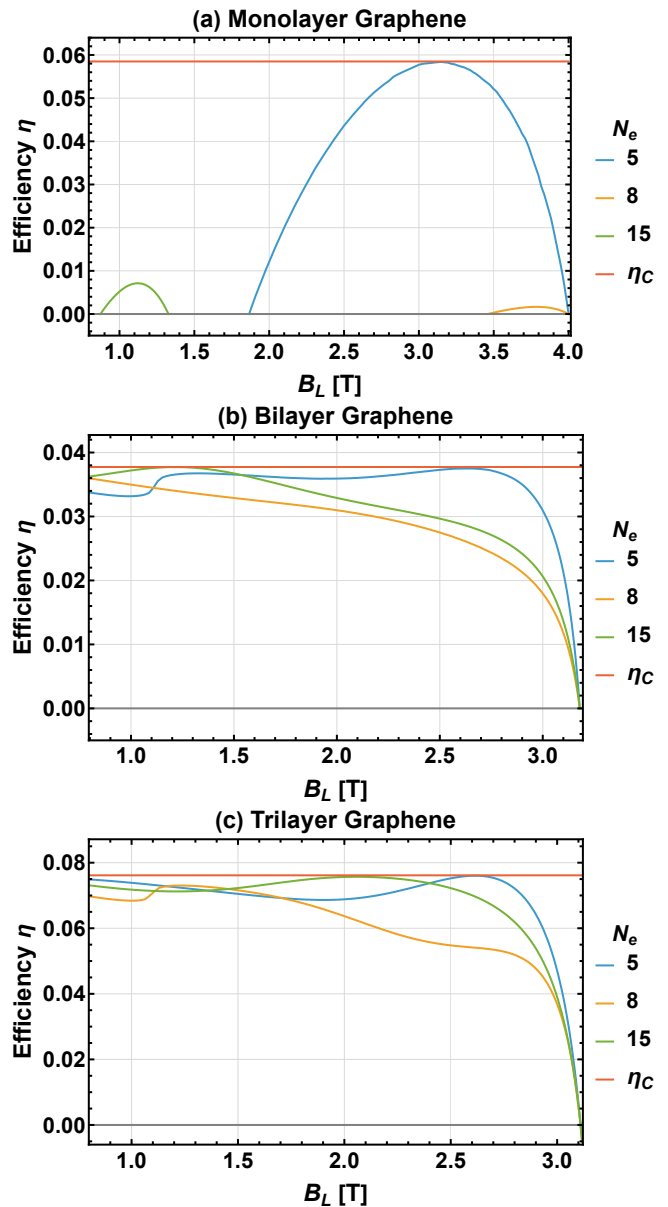


FIG. 6: Stirling engine efficiency η as a function of the low magnetic field B_L for (a) monolayer, (b) bilayer, and (c) trilayer graphene. Each panel shows results for $N_e = 5, 8, 15$ and the Carnot bound η_C . Parameters are: (a) $T_L = 50.7$ K, $T_H = 53.85$ K, $B_H = 4.0$ T, $\eta_C = 0.058$; (b) $T_L = 45.9$ K, $T_H = 47.7$ K, $B_H = 3.18$ T, $\eta_C = 0.037$; (c) $T_L = 18.2$ K, $T_H = 19.7$ K, $B_H = 3.11$ T, $\eta_C = 0.078$.

of $\eta_C \simeq 0.06$, with the high magnetic field fixed at $B_H = 4.0$ T. Although some curves (e.g., $N_e = 5$) can, in principle, achieve the Carnot limit with finite work, this only occurs at low carrier densities and within narrow B_L intervals. Outside these regions, the device switches to other operational regime modes, and the definition of efficiency is not well-defined. It is for this reason that only small intervals where the substance operates as an engine exist, while no efficiency curves are observed be-

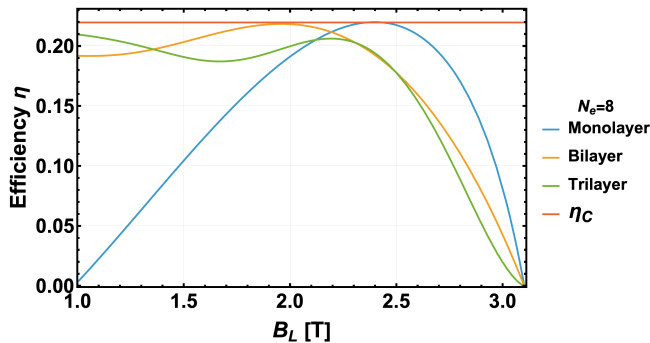


FIG. 7: Stirling engine efficiency η as a function of the low magnetic field B_L at fixed high field $B_H = 3.1$ T. Reservoir temperatures are set to $T_L = 21.3$ K, $T_H = 27.3$ K for the monolayer; $T_L = 16.7$ K, $T_H = 21.4$ K for the bilayer; and $T_L = 10.0$ K, $T_H = 12.9$ K for the trilayer. In all cases, the Carnot efficiency is $\eta_C = 0.22$.

yond them.

This restricted behavior can be interpreted as a consequence of the large spacing between relativistic Landau levels, which limits the thermal accessibility of higher-energy states. As a result, the heat exchanged during the isothermal strokes, while retaining the correct sign for engine operation, becomes smaller in magnitude. When the heat contribution from the isomagnetic strokes surpasses that of the isothermal ones—an effect enhanced by the Landau level separation—the net work output turns negative, and the cycle ceases to function as an engine. These exotic behaviors associated with monolayer graphene will be discussed in later sections.

For the bilayer graphene in Fig. 6(b), the system operates as an engine across the entire B_L range considered, with the high magnetic field fixed at $B_H = 3.18$ T. The thermal reservoirs are maintained at $T_L = 45.9$ K and $T_H = 47.7$ K, corresponding to a Carnot efficiency of $\eta_C \simeq 0.04$. Under these conditions, the curves for $N_e = 5$ and $N_e = 15$ attain the Carnot bound at finite values of B_L , with the $N_e = 15$ case attaining η_C at lower B_L values than $N_e = 5$. In contrast, the $N_e = 8$ curve remains slightly below η_C over the full range, exhibiting a broad maximum just under the Carnot line at $B_L \simeq 0.8$ [T]. This reflects a more balanced competition between the isothermal and isomagnetic contributions arising from the parametrization of the chemical potential. This intermediate behavior highlights how the bilayer spectrum, with its linear scaling in B , provides a broader operational window: depending on the carrier number, the cycle can either saturate the Carnot limit or remain close to it with finite work output. This behavior contrasts with results for twisted bilayer graphene studied within the canonical ensemble [56]. While such systems can reach Carnot efficiency in Otto cycles [50] and exhibit high efficiencies in quantum Stirling cycles, saturation of the Carnot bound in the Stirling cycle has not been reported in that framework. This suggests that

a Fermi–Dirac description with fixed particle number enhances thermodynamic performance in graphene-based quantum heat engines, highlighting the role of ensemble choice and carrier-number constraints in setting efficiency limits.

For the trilayer graphene in Fig. 6(c), the high magnetic field is fixed at $B_H = 3.11$ T, while the thermal reservoirs are set at $T_L = 18.2$ K and $T_H = 19.7$ K with a Carnot efficiency $\eta_C \simeq 0.08$. Under these conditions, the $N_e = 15$ curve reaches the Carnot bound near $B_L \simeq 2.1$ T, whereas the $N_e = 5$ case attains η_C at $B_L \simeq 2.65$ T, closer to the upper field value $B_H = 3.18$ T. In contrast, the $N_e = 8$ curve remains consistently lower across the full range, exhibiting a broad maximum well below η_C . This behavior indicates that the enhanced zero-mode degeneracy and the steeper $B^{3/2}$ scaling of the spectrum restrict the proximity to reversible performance, with the sharpness of the response being induced by the parametrization of the chemical potential. Overall, this smoother yet less favorable trend demonstrates that, although trilayer graphene can reach Carnot efficiency for specific carrier numbers, its operational window in temperature space is narrower than in the bilayer case, and the efficiency maxima are more sensitive to the choice of N_e .

The purpose of Fig. 6 is to demonstrate, over a common range of magnetic field values, that all stacking configurations considered here are capable of reaching the Carnot efficiency. The comparison was designed such that, for each stacking, at least one of the selected particle numbers N_e attains η_C within approximately the same efficiency window. Because this requires employing similar operational temperatures across the panels, the resulting efficiencies in Fig. 6 appear relatively small. The main motivation behind this choice is to provide a direct and uniform demonstration that the Carnot bound can, in principle, be achieved in all cases, irrespective of the stacking.

In contrast, Fig. 7 focuses on the case $N_e = 8$, where all stacking configurations operate as an engine with the same fixed high magnetic field $B_H = 3.1$ T. The thermal reservoirs are chosen such that for the monolayer the temperatures are $T_L = 21.3$ K and $T_H = 27.3$ K, for the bilayer $T_L = 16.7$ K and $T_H = 21.4$ K, and for the trilayer $T_L = 10.0$ K and $T_H = 12.9$ K. Despite these differences, all three cases correspond to the same Carnot efficiency, $\eta_C \simeq 0.22$.

This configuration highlights the role of carrier density in shaping the operational regime. For the trilayer, the maximum efficiency nearly reaches the Carnot limit as $B_L \rightarrow 1.0$ T (the lowest field considered), whereas for the monolayer it occurs at higher fields, around $B_L \simeq 2.4$ T. The bilayer exhibits an intermediate response, achieving the Carnot limit near $B_L \simeq 1.9$ T. Compared to Fig. 6, which employed a uniform B_L range to demonstrate that Carnot efficiency can be reached across all stackings, the present figure emphasizes how the optimal field for reversible operation shifts significantly between systems.

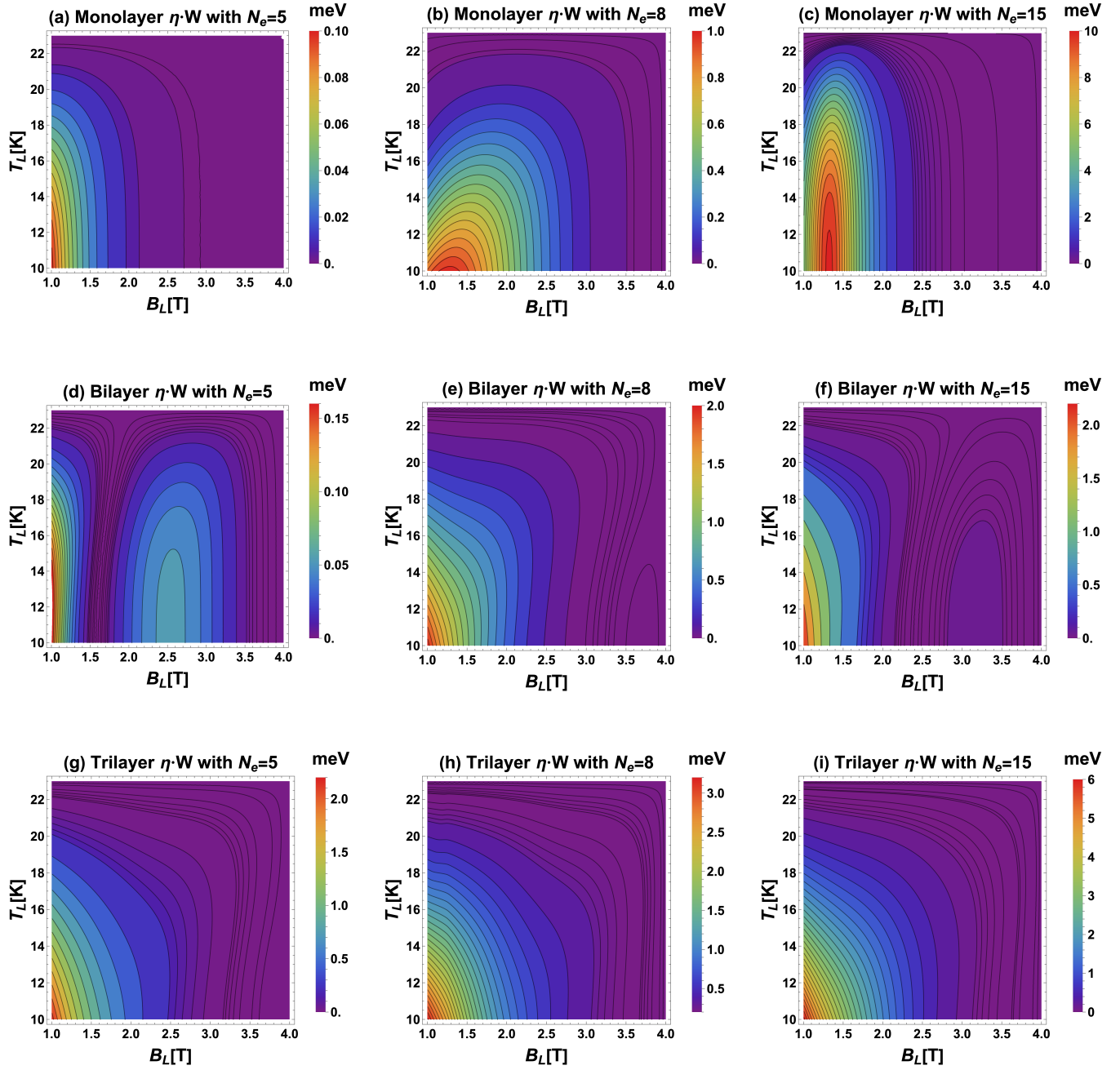


FIG. 8: Contour plots of the product $\eta \cdot W$ as a function of the low parameters B_L and T_L , with fixed high parameters $T_H = 23$ K and $B_H = 4$ T. The panels correspond to monolayer (a)-(c), bilayer (d)-(e) and trilayer (g)-(i) graphene with (left) $N_e = 5$, (center) $N_e = 8$, and (right) $N_e = 15$.

This contrast underscores the crucial interplay between the Landau-level spectrum and the chemical potential in determining the precise conditions under which Carnot efficiency is realized.

B. Stirling Maximum Gain

In Sec. IV A, it was shown that different graphene stackings can reach Carnot efficiency for distinct particle numbers and thermal reservoirs. However, achieving maximum efficiency does not necessarily imply maximizing the extracted work. For this reason, this section analyzes the maximum gain, defined as the product $\eta \cdot W$

(useful work), as a function of particle number and stacking configuration, while keeping the reservoirs fixed and sweeping over the same magnetic-field range. To illustrate this behavior, Fig. 8 displays contour maps of ηW as functions of the low parameters B_L and T_L , with the hot bath fixed at $T_H = 23$ K and $B_H = 4.0$ T. The rows correspond to monolayer, bilayer, and trilayer graphene, while the columns show the cases $N_e \in \{5, 8, 15\}$. In all configurations, the best performance is concentrated at low magnetic fields ($B_L \lesssim 1.5$ T) and moderately low temperatures ($T_L \sim 10$ – 15 K), reflecting the enhancement of work and efficiency in regimes where a denser set of thermally accessible Landau levels is available.

In the monolayer case, shown in Figs. 8(a)–(c), the high- ηW region is narrow and quickly suppressed as either B_L or T_L increase. The maximum for $N_e = 5$ occurs at the lowest field and within $T_L \in 10$ – 13 K. For $N_e = 8$, the favorable region expands slightly in field range ($B_L \in 1.0$ – 1.5 T) but narrows in temperature ($T_L \in 10$ – 11 K). At $N_e = 15$, the contour shrinks again in field range relative to $N_e = 8$, though it widens in temperature ($T_L \in 10$ – 14 K). The maximum values also increase markedly with particle number, from about 0.1 meV at $N_e = 5$ to 1.0 meV at $N_e = 8$, and nearly 10 meV at $N_e = 15$.

For bilayer graphene, illustrated in Figs. 8(d)–(f), the optimum broadens into a smoother, rounded peak, indicating a wider operational window consistent with the enhanced density of states. For $N_e = 5$, the maximum again appears near the lowest field but over a broader temperature range ($T_L \simeq 10$ – 15 K), together with a secondary plateau around $B_L \simeq 2.5$ T. For $N_e = 8$, the maximum shifts back to very low fields and a narrow window of $T_L \simeq 10$ – 11 K. At $N_e = 15$, the contours resemble the previous case but display a low- ηW pocket at $B_L \simeq 2.8$ – 3.4 T. The scaling with particle number differs from the monolayer: the maxima are 0.15 meV for $N_e = 5$, 2.0 meV for $N_e = 8$, but remain at 2.0 meV for $N_e = 15$, showing saturation rather than continued growth.

The trilayer configuration, depicted in Figs. 8(g)–(i), sustains sizable values of ηW over a comparable B_L range and extends to slightly higher T_L . At $N_e = 5$, the maximum is located near the lowest field and around $T_L \simeq 10$ K, reaching 2.0 meV. For $N_e = 8$, the contours broaden both in field and temperature, with the maximum increasing to 3.0 meV. At $N_e = 15$, the pattern closely resembles the $N_e = 8$ case but with a higher maximum of about 6.0 meV, still significantly smaller than the monolayer for the same particle number. This reduction is a direct consequence of the smaller Landau-level spacing and lower energy scale in the trilayer system.

C. Stirling Operational Regimes

In the previous sections, the working substances were shown to operate as engines with high efficiency and sig-

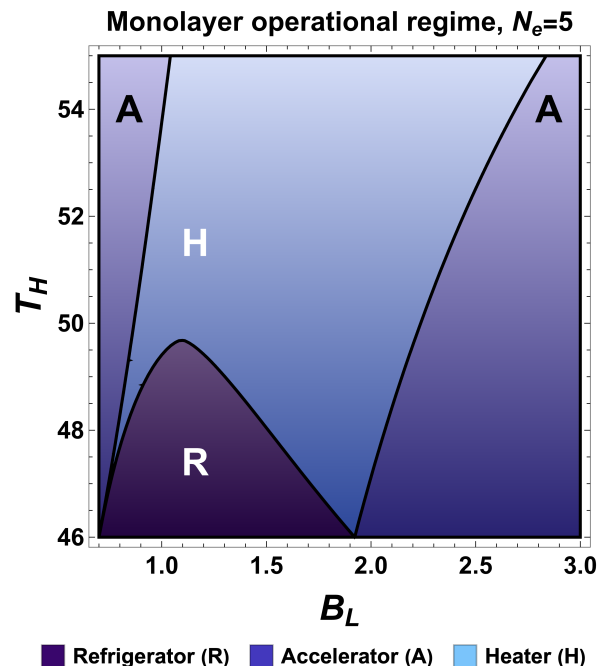


FIG. 9: Operational regimes of the Stirling cycle for monolayer graphene with $N_e = 5$, as functions of the low magnetic field B_L and hot reservoir temperature T_H , at fixed $B_H = 3.0$ T and $T_L = 46$ K.

nificant work extraction. Nevertheless, these systems may also exhibit exotic behavior, leading to the emergence of distinct operational regimes. To illustrate this point, Fig. 9 presents the operational map of the Stirling cycle for monolayer graphene at fixed $B_H = 3.0$ T, $T_L = 46$ K, and $N_e = 5$. Within the explored window of low magnetic field B_L and hot reservoir temperature T_H , no engine region is observed. Instead, the diagram reveals a small refrigerator domain at $B_L \simeq 0.7$ – 1.8 T and $T_H \simeq 46$ – 49.5 K, two accelerator wedges near the lowest and highest values of B_L , and a broad heater region covering most of the parameter space.

The absence of engine operation indicates that, under these conditions, heat exchange in the isomagnetic strokes dominates over the isothermal contributions. This outcome reflects both the wide spacing of relativistic Landau levels and the parametrized chemical potential imposed to maintain $N_e = 5$ throughout the cycle. Consequently, the system exhibits $W < 0$ across the entire diagram, with the specific regime determined by the balance of heat flows: refrigerator, accelerator, or heater. These results align with the performance maps in Fig. 8, where the monolayer shows weak ηW values and a rapidly vanishing optimum, as well as with the efficiency curves in Fig. 6, which display only small, low-efficiency engine regions and predominantly non-engine behavior. Engine windows may emerge under different parameter choices, but are absent in the present configuration.

This does not exclude bilayer graphene from exhibiting the full range of operational regimes. Previous studies

have shown that the same Stirling cycle implemented in bilayer graphene can display all operational regimes under different parameter choices and when the chemical potential is not fixed [56]. Their absence here therefore reflects the specific thermodynamic window considered, rather than an intrinsic limitation of the system.

It should be emphasized that realizing different operational regimes in bilayer and trilayer graphene would require substantially lower temperatures and much higher magnetic fields than those explored in this study, owing to their smaller characteristic energy scales. Accordingly, the present analysis focuses on regimes accessible at higher temperatures, which are not only more relevant to this work but also more feasible from an experimental perspective.

At the same time, it is important to note that the present analysis is intended as a theoretical proof of concept rather than a concrete experimental proposal. While the main text focuses on a fixed-particle-number formulation in order to enable a controlled comparison between different multilayer systems, an alternative and experimentally natural realization of the Stirling cycle consists in fixing the chemical potential. This extension, which mimics the situation of a graphene system coupled to electronic reservoirs, is explicitly addressed in Appendix A, where we show that the qualitative features of the operational regimes remain robust with respect to the choice of thermodynamic ensemble.

In a realistic implementation, field-driven modifications of the Landau-level structure would induce variations of the sample magnetization across the different strokes of the cycle. When the graphene system is electromagnetically coupled to an external circuit, these magnetization changes can generate an electromotive response, allowing the conversion of field-induced energy variations into usable electrical work. This mechanism provides a physically consistent route for work extraction without requiring commitment to a specific device architecture.

V. CONCLUSIONS AND DISCUSSION

This study investigates quantum Stirling cycles in monolayer, AB-stacked bilayer, and ABC-stacked trilayer graphene subjected to perpendicular magnetic fields. Using a grand-canonical, fully fermionic framework based on exact Landau spectra, we demonstrate that the cycles can operate within experimentally accessible regimes. This is supported by an order-of-magnitude comparison between simulated particle numbers, chemical potentials, and sheet carrier densities defined by the magnetic length.

Thermodynamic quantities, including internal energy and entropy, were consistently evaluated using Fermi-Dirac statistics, with the chemical potential $\mu(T, B)$ parametrized to conserve particle number along both isothermal and isomagnetic branches. In this frame-

work, the perpendicular magnetic field acted as the external control parameter driving the cycle.

Across the explored parameter space and for multiple fixed particle numbers, the monolayer and the stacked configurations demonstrated the capacity to reach Carnot efficiency under suitable magnetic conditions. Among them, the AB bilayer exhibited the broadest operational window and reached the Carnot bound while sustaining finite work output, whereas the monolayer showed more constrained operation and the trilayer presented smoother efficiency trends with sizable values of the combined performance metric ηW over a comparable B_L range.

Overall, the monolayer Stirling cycle, due to its larger Landau-level spacing and higher characteristic energy scale, delivered greater useful work at higher efficiency compared with the bilayer and trilayer cases. Its capability to operate across all thermodynamic regimes as an engine, refrigerator, heater, and accelerator highlights its versatility. This feature suggests possible applications, such as employing the monolayer cycle to cool other working substances including quantum batteries or supercondensates, while simultaneously acting as a heater at elevated temperatures.

Our comparative analysis shows that the efficiency and work output of a Stirling cycle are strongly influenced by the stacking-dependent Landau-level structure of graphene multilayers. This demonstrates that simply varying the layer configuration introduces distinct thermodynamic behaviors and efficiency profiles, proving that novel effects can be engineered without altering the intrinsic material composition. Remarkably, certain parameter regimes allow the cycle to approach Carnot efficiency while retaining finite work, a behavior that emerges solely from the intrinsic spectral properties of each stacking. These results highlight stacking order as a meaningful design knob for tailoring the thermodynamic response of quantum heat engines.

ACKNOWLEDGMENTS

B.C, F.J.P., M.H.G, N.C, and P.V. acknowledge financial support from ANID Fondecyt grant no. 1240582. B.C, F.J.P., M.H.G, and P.V. acknowledge financial support from ANID Fondecyt grant no. 1250173. B.C acknowledge PUCV and Programa de Incentivo a la Iniciación Científica (PIIC) no. 004 from "Dirección de Postgrado" of UTFSM. B.C. acknowledges the support of ANID Becas/Doctorado Nacional 21250015. C.L. thanks the support by the Brazilian agencies CNPq and FAPERJ. M.H.G acknowledge PUCV and "Dirección de Postgrado" of UTFSM.

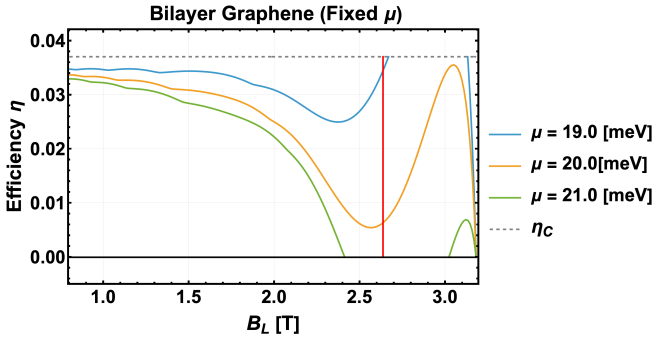


FIG. 10: Stirling-cycle efficiency η of AB-stacked bilayer graphene as a function of the lower magnetic field B_L , computed at fixed chemical potential $\mu = 19, 20$, and 21 meV. The cycle parameters are the same as those used in the main text: $T_L = 45.9$ K, $T_H = 47.7$ K, and $B_H = 3.18$ T, corresponding to a Carnot efficiency $\eta_C = 0.037$ (horizontal dashed line). The vertical red line marks the value of B_L at which the fixed-particle-number protocol with $N_e = 5$ yields $\eta = \eta_C$ in the main analysis. For values exceeding η_C or falling below zero, the system transitions to a different operational regime.

Appendix A: Stirling cycle at fixed chemical potential

In the main text, the Stirling cycle was primarily formulated under a fixed-particle-number constraint, with the chemical potential determined self-consistently as $\mu = \mu(T, B)$. An alternative and experimentally natural formulation consists in fixing the chemical potential throughout the cycle, corresponding to a graphene system coupled to an electronic reservoir. In this Appendix, we present additional results obtained within this fixed- μ formulation in order to assess the robustness of the conclusions reported in the main text.

1. Efficiency and work at fixed μ

We first analyze the Stirling-cycle efficiency and total work per cycle for AB-stacked bilayer graphene by keeping the chemical potential fixed during the entire cycle. The bilayer system is chosen here because it exhibits the broadest operational window in the fixed- N_e analysis discussed in the main text.

Fig. 10 shows the efficiency η as a function of the lower magnetic field B_L for several representative values of μ , using the same cycle parameters as in the main text, $T_L = 45.9$ K, $T_H = 47.7$ K, and $B_H = 3.18$ T, for which the Carnot efficiency is $\eta_C = 0.037$. The vertical red line indicates the value of B_L at which the fixed-particle-number protocol with $N_e = 5$ attains $\eta = \eta_C$. For values below zero and above η_C , the definition of efficiency is no longer applicable because the system transitions to a different operational regime. To avoid possible confusion, these regions are therefore not plotted.

At fixed μ , both the efficiency and the extracted work

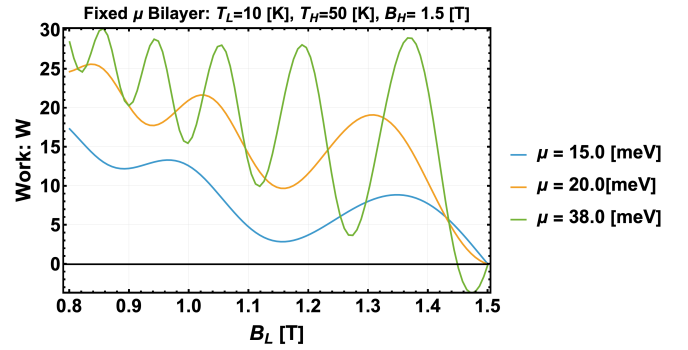


FIG. 11: Total work per cycle W for AB-stacked bilayer graphene as a function of the lower magnetic field B_L , computed at fixed chemical potential $\mu = 15, 20$, and 38 meV. The cycle parameters are $T_L = 10$ K, $T_H = 50$ K, and $B_H = 1.5$ T. The oscillatory behavior originates from successive crossings of the chemical potential through the Landau levels, which modulate the electronic population and the heat exchanged during the isothermal strokes. For value falling below zero, the system transitions to a different operational regime.

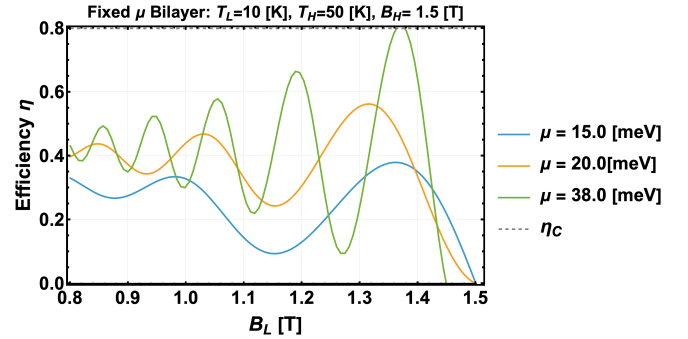


FIG. 12: Stirling-cycle efficiency η of AB-stacked bilayer graphene as a function of the lower magnetic field B_L , computed at fixed chemical potential $\mu = 15, 20$, and 38 meV, using the same cycle parameters as in Fig. 11. The horizontal dashed line indicates the Carnot efficiency η_C . Despite the oscillatory features induced by the crossings of the chemical potential through the Landau levels, well-defined high-efficiency operating regimes persist. For values falling η_C below zero, the system transitions to a different operational regime.

exhibit oscillatory structures as functions of B_L , as shown in Figs. 12 and 11. These oscillations originate from successive Landau-level crossings through the fixed chemical potential, which modulate the electronic population and, consequently, the heat exchanged during the isothermal strokes. Despite these quantitative differences with respect to the fixed- N_e formulation, well-defined operating windows with sizable work output and high efficiency persist. This confirms that the qualitative behavior of the bilayer Stirling engine is not an artifact of the ensemble choice.

2. Particle-number variation at fixed μ

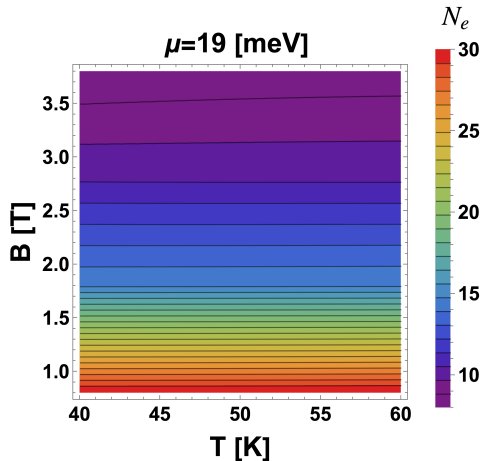


FIG. 13: Contour plot of the particle number N_e as a function of temperature T and magnetic field B for AB-stacked bilayer graphene at fixed chemical potential $\mu = 19$ meV. The parameter range corresponds to that used in the main text. In this region, the nearly horizontal contour lines indicate that the particle number varies only weakly with temperature, explaining the consistency between the fixed- N_e and fixed- μ formulations in the operating regime of interest.

To further clarify the relation between the fixed- N_e and fixed- μ formulations, Fig. 13 presents a contour plot of the particle number N_e as a function of temperature T and magnetic field B at fixed chemical potential $\mu = 19$ meV. The parameters correspond to the same range used in the main text.

In this parameter range, the particle number exhibits only weak variations with temperature, as indicated by the nearly horizontal contour lines. This shows that, close to the operating point relevant for the Stirling cycle, fixing μ effectively corresponds to an approximately constant particle number. This explains why the fixed- N_e and fixed- μ formulations yield consistent results in the regime explored in the main text.

Overall, the analysis presented in this Appendix demonstrates that the performance and operational regimes of the bilayer graphene Stirling engine are robust with respect to the choice of thermodynamic ensemble, and that the main conclusions of the manuscript are rooted in the underlying Landau-level structure rather than in a particular constraint on μ or N_e .

-
- [1] S. Vinjanampathy and J. Anders, Quantum thermodynamics, *Contemporary Physics* **57**, 545 (2016).
- [2] R. Kosloff, Quantum thermodynamics: A dynamical viewpoint, *Entropy* **15**, 2100 (2013).
- [3] S. Deffner and S. Campbell, *Quantum Thermodynamics: An Introduction to the Thermodynamics of Quantum Information* (Morgan & Claypool Publishers, San Rafael - USA, 2019).
- [4] J. Millen and A. Xuereb, Perspective on quantum thermodynamics, *New J. Phys.* **18**, 011002 (2016).
- [5] F. Binder, S. Vinjanampathy, K. Modi, and J. Goold, Quantum thermodynamics of general quantum processes, *Phys. Rev. E* **91**, 032119 (2015).
- [6] F. Binder, L. A. Correa, C. Gogolin, J. Anders, and G. Adesso, Thermodynamics in the quantum regime, in *Fundamental Theories of Physics*, Vol. 195 (Springer, New York, 2018).
- [7] N. M. Myers, O. Abah, and S. Deffner, Quantum thermodynamic devices: From theoretical proposals to experimental reality, *AVS Quantum Science* **4**, 027101 (2022).
- [8] G. L. Zanin, T. Haffner, M. A. A. Talarico, E. I. Duzzioni, P. H. Souto Ribeiro, G. T. Landi, and L. C. Celeri, Experimental quantum thermodynamics with linear optics, *Braz. J. Phys.* **49**, 783 (2019).
- [9] C. H. S. Vieira, J. L. D. de Oliveira, J. F. G. Santos, P. R. Dieguez, and R. M. Serra, Exploring quantum thermodynamics with NMR, *J. Magn. Reson. Open* **16-17**, 100105 (2023).
- [10] G. De Chiara, G. Landi, A. Hewgill, B. Reid, A. Ferraro, A. J. Roncaglia, and M. Antezza, Reconciliation of quantum local master equations with thermodynamics, *New J. Phys.* **20**, 113024 (2018).
- [11] B. Castorene, F. J. Peña, A. Norambuena, S. E. Ulloa, C. Araya, and P. Vargas, Entropy, entanglement, and susceptibility of three qubits near quantum criticality, *Phys. Rev. E* **111**, 034118 (2025).
- [12] P. Liuzzo-Scorpo, L. A. Correa, R. Schmidt, and G. Adesso, Thermodynamics of quantum feedback cooling, *Entropy* **18**, 48 (2016).
- [13] F. Brandao, M. Horodecki, N. Ng, J. Oppenheim, and S. Wehner, The second laws of quantum thermodynamics, *Proc. Natl. Acad. Sci. U.S.A.* **112**, 3275 (2015).
- [14] M. Esposito, R. Kawai, K. Lindenberg, and C. Van den Broeck, Quantum-dot Carnot engine at maximum power, *Phys. Rev. E* **81**, 041106 (2010).
- [15] P. A. Erdman, F. Mazza, R. Bosisio, G. Benenti, R. Fazio, and F. Taddei, Thermoelectric properties of an interacting quantum dot based heat engine, *Phys. Rev. B* **95**, 245432 (2017).
- [16] M. Josefsson, A. Svilans, A. M. Burke, E. A. Hoffmann, S. Fahlvik, C. Thelander, M. Leijnse, and H. Linke, A quantum-dot heat engine operating close to the thermodynamic efficiency limits, *Nat. Nanotech.* **13**, 920 (2018).
- [17] M. Josefsson, A. Svilans, H. Linke, and M. Leijnse, Optimal power and efficiency of single quantum dot heat engines: Theory and experiment, *Phys. Rev. B* **99**, 235432 (2019).
- [18] M. Josefsson and M. Leijnse, Double quantum-dot engine fueled by entanglement between electron spins, *Phys. Rev. B* **101**, 081408 (2020).

- [19] J. Du, W. Shen, X. Zhang, S. Su, and J. Chen, Quantum-dot heat engines with irreversible heat transfer, *Phys. Rev. Research* **2**, 013259 (2020).
- [20] H. Saygin and A. Sisman, Quantum degeneracy effect on the work output from a Stirling cycle, *J. Appl. Phys.* **90**, 3086 (2001).
- [21] A. Sisman and H. Saygin, Efficiency analysis of a Stirling power cycle under quantum degeneracy conditions, *Phys. Scr.* **63**, 263 (2001).
- [22] C. Cruz, H.-R. Rastegar-Sedehi, M. F. Anka, T. R. de Oliveira, and M. Reis, Quantum Stirling engine based on dinuclear metal complexes, *Quantum Science and Technology* **8**, 035010 (2023).
- [23] S. H. Raja, S. Maniscalco, G.-S. Paraoanu, J. P. Pekola, and N. Lo Gullo, Finite-time quantum Stirling heat engine, *New J. Phys.* **23**, 033034 (2021).
- [24] S. Cakmak and H. R. R. Sedehi, Construction of a quantum Stirling engine cycle tuned by dynamic-angle spinning, *Phys. Scr.* **98**, 105921 (2023).
- [25] B. Castorene, F. J. Pena, A. Norambuena, S. E. Ulloa, C. Araya, and P. Vargas, Effects of magnetic anisotropy on three-qubit antiferromagnetic thermal machines, *Phys. Rev. E* **110**, 044135 (2024).
- [26] F. Wu, L. Chen, F. Sun, C. Wu, and Y. Zhu, Performance and optimization criteria for forward and reverse quantum Stirling cycles, *ENERGY CONVERSION AND MANAGEMENT* **39**, 733 (1998).
- [27] H.-R. Rastegar-Sedehi, N. Papadatos, and C. Cruz, Universal quantum Stirling-like engine under squeezed thermal baths, *EUROPEAN PHYSICAL JOURNAL PLUS* **140**, 199 (2025).
- [28] Z. Huang, F. Wu, L. Chen, C. Wu, and F. Guo, Performance optimization for an irreversible quantum Stirling cooler, *JOURNAL OF THERMAL SCIENCE* **11**, 193 (2002).
- [29] P. D. Li, G. Y. Ding, J. Q. Zhang, Q. Yuan, S. Q. Dai, T. H. Cui, F. Zhou, L. Chen, Q. Zhong, H. Jing, S. K. Ozdemir, and M. Feng, Experimental demonstration of single-spin Stirling engine cycles with enhanced efficiency, *Phys. Rev. A* **111**, L010203 (2025).
- [30] C. Araya, F. J. Pena, A. Norambuena, B. Castorene, and P. Vargas, Magnetic Stirling cycle for qubits with anisotropy near the quantum critical point, *TECHNOLOGIES* **11**, 169 (2023).
- [31] S. Chatterjee, A. Koner, S. Chatterjee, and C. Kumar, Temperature-dependent maximization of work and efficiency in a degeneracy-assisted quantum Stirling heat engine, *Phys. Rev. E* **103**, 062109 (2021).
- [32] S. Koyanagi and Y. Tanimura, Thermodynamic quantum Fokker-Planck equations and their application to thermostatic Stirling engine, *J. Chem. Phys.* **161**, 112501 (2024).
- [33] F. J. Peña, O. Negrete, G. Alvarado-Barrios, D. Zambrano, A. González, A. S. Nunez, P. A. Orellana, and P. Vargas, Magnetic Otto engine for an electron in a quantum dot: Classical and quantum approach, *Entropy* **21**, 512 (2019).
- [34] S. Deffner, Efficiency of harmonic quantum Otto engines at maximal power, *Entropy* **20**, 875 (2018).
- [35] A. H. Castro Neto, F. Guinea, N. M. Peres, K. S. Novoselov, and A. K. Geim, The electronic properties of graphene, *Rev. Mod. Phys.* **81**, 109 (2009).
- [36] E. McCann and V. I. Fal'ko, Landau-level degeneracy and quantum Hall effect in a graphite bilayer, *Phys. Rev. Lett.* **96**, 086805 (2006).
- [37] H. Min and A. H. MacDonald, Electronic Structure of Multilayer Graphene, *Progress of Theoretical Physics Supplement* **176**, 227 (2008).
- [38] S. Yuan, R. Roldán, and M. I. Katsnelson, Landau level spectrum of ABA- and ABC-stacked trilayer graphene, *Phys. Rev. B* **84**, 125455 (2011).
- [39] M. O. Goerbig, Electronic properties of graphene in a strong magnetic field, *Rev. Mod. Phys.* **83**, 1193 (2011).
- [40] M. Koshino and T. Ando, Magneto-optical properties of multilayer graphene, *Phys. Rev. B* **77**, 115313 (2008).
- [41] M. Nakamura and L. Hirasawa, Electric transport and magnetic properties in multilayer graphene, *Phys. Rev. B* **77**, 045429 (2008).
- [42] V. Ghai, S. Pashazadeh, H. Ruan, and R. Kadar, Orientation of graphene nanosheets in magnetic fields, *PROGRESS IN MATERIALS SCIENCE* **143**, 101251 (2024).
- [43] F. P. Rizzo, S. Vizcaya, E. Menendez-Proupin, J. M. Florez, L. Chico, and E. S. Morell, Behavior of localized states in double twisted ABC trilayer graphene, *Carbon* **222**, 118952 (2024).
- [44] P. Rickhaus, M. Weiss, L. Marot, and C. Schoenberger, Quantum Hall effect in graphene with superconducting electrodes, *Nano Lett.* **12**, 1942 (2012).
- [45] W. Bao, L. Jing, J. Velasco Jr, Y. Lee, G. Liu, D. Tran, B. Standley, M. Aykol, S. Cronin, D. Smirnov, *et al.*, Stacking-dependent band gap and quantum transport in trilayer graphene, *Nat. Phys.* **7**, 948 (2011).
- [46] K. S. Novoselov, Z. Jiang, Y. Zhang, S. V. Morozov, H. L. Stormer, U. Zeitler, J. C. Maan, G. S. Boebinger, P. Kim, and A. K. Geim, Room-temperature quantum Hall effect in graphene, *Science* **315**, 1379 (2007).
- [47] Y. Kayanuma and H. Nakayama, Nonadiabatic transition at a level crossing with dissipation, *Phys. Rev. B* **57**, 13099 (1998).
- [48] X. Dai, R. Trappen, H. Chen, D. Melanson, M. A. Yurtalan, D. M. Tennant, A. J. Martinez, Y. Tang, E. Mozgunov, J. Gibson, J. A. Grover, S. M. Disseler, J. I. Basham, S. Novikov, R. Das, A. J. Melville, B. M. Niedzielski, C. F. Hirjibehedin, K. Serniak, S. J. Weber, J. L. Yoder, W. D. Oliver, K. M. Zick, D. A. Lidar, and A. Lupascu, Dissipative Landau-Zener tunneling in the crossover regime from weak to strong environment coupling, *Nat. Commun.* **16**, 329 (2025).
- [49] A. Mani, S. Pal, and C. Benjamin, Designing a highly efficient graphene quantum spin heat engine, *Scientific Reports* **9**, 6018 (2019).
- [50] A. Singh and C. Benjamin, Magic angle twisted bilayer graphene as a highly efficient quantum Otto engine, *Phys. Rev. B* **104**, 125445 (2021).
- [51] N. M. Myers, F. J. Peña, N. Cortés, and P. Vargas, Multilayer graphene as an endoreversible Otto engine, *Nanomaterials* **13**, 1548 (2023).
- [52] O. Arroyo-Gascon, R. Fernandez-Perea, E. S. Morell, C. Cabrillo, and L. Chico, Universality of moiré physics in collapsed chiral carbon nanotubes, *Carbon* **205**, 394 (2023).
- [53] N. G. Kalugin, L. Jing, E. Suarez Morell, G. C. Dyer, L. Wickey, M. Ovezmyradov, A. D. Grine, M. C. Wanke, E. A. Shaner, C. N. Lau, L. E. F. Foa Torres, M. V. Fistul, and K. B. Efetov, Photoelectric polarization-sensitive broadband photoresponse from interface junction states in graphene, *2D Mater.* **4**, 015002 (2017).
- [54] M. Pelc, E. Suarez Morell, L. Brey, and L. Chico, Elec-

- tronic conductance of twisted bilayer nanoribbon flakes, *J. Phys. Chem. C* **119**, 10076 (2015).
- [55] E. Suarez Morell and L. E. F. Foa Torres, Radiation effects on the electronic properties of bilayer graphene, *Phys. Rev. B* **86**, 125449 (2012).
- [56] H. M. Soufy and C. Benjamin, Enhanced performance across Otto, Carnot, and Stirling cycles revealed by flat-band thermodynamics, *Phys. Rev. A* **112**, 052215 (2025).
- [57] F. J. Peña, D. Zambrano, O. Negrete, G. De Chiara, P. A. Orellana, and P. Vargas, Quasistatic and quantum-adiabatic Otto engine for a two-dimensional material: The case of a graphene quantum dot, *Phys. Rev. E* **101**, 012116 (2020).
- [58] J. Pan, H. Zhang, Y. Zheng, B. Zhang, T. Zhang, and P. Sheng, Spatial variation of charge carrier density in graphene under a large bias current, *Phys. Rev. B* **93**, 115424 (2016).
- [59] S. L. Moore, M. S. Sánchez, M. C. Strasbourg, Y. Shao, J. Pack, Y. Wang, D. J. Rizzo, B. S. Jessen, M. Cothrine, D. G. Mandrus, T. Taniguchi, K. Watanabe, K. S. Burch, C. R. Dean, J. Hone, M. Fogler, A. J. Millis, A. Rubio, P. J. Schuck, T. Stauber, and D. N. Basov, Collective modes in multilayer graphene/ α -RuCl₃ heterostructures, *Phys. Rev. X* **15**, 041011 (2025).
- [60] K. J. U. Vidarte and C. Lewenkopf, High-energy Landau levels in graphene beyond nearest-neighbor hopping processes: Corrections to the effective Dirac Hamiltonian, *Phys. Rev. B* **106**, 155414 (2022).
- [61] K. S. Novoselov, A. K. Geim, S. V. Morozov, D. Jiang, M. I. Katsnelson, I. V. Grigorieva, S. V. Dubonos, and A. A. Firsov, Two-dimensional gas of massless dirac fermions in graphene, *Nature* **438**, 197 (2005).
- [62] M.-H. Liu, Theory of carrier density in multigated doped graphene sheets with quantum correction, *Phys. Rev. B* **87**, 125427 (2013).
- [63] H.-R. Rastegar-Sedehi and C. Cruz, Exploring entanglement effects in a quantum Stirling heat engine, *Phys. Scr.* **99**, 125936 (2024).
- [64] B. Castorene, V. G. de Paula, F. J. Pena, C. Cruz, M. Reis, and P. Vargas, Quantum level-crossing induced by anisotropy in spin-1 Heisenberg dimers: Applications to quantum Stirling engines, *Adv. Quantum Technol.* **8**, e2500204 (2025).
- [65] G. Behrendt and S. Deffner, Endoreversible Stirling cycles: Plasma engines at maximal power, *Entropy* **27**, 807 (2025).